Aline Kirsten Vidal de Oliveira

AUTOMATIC FAULT DETECTION OF PHOTOVOLTAIC SOLAR GENERATORS APPLYING AERIAL INFRARED THERMOGRAPHY

Qualificação para passagem direta ao doutorado submetida ao Programa de Pós-Graduação em Engenharia Civil da Universidade Federal de Santa Catarina para a obtenção do Grau de Doutor em Engenharia Civil
Orientador: Prof. Ricardo Rüther, Ph.D.
Coorientador: Dr. Mahammedreza Aghaei

Florianópolis
2018

Aline Kirsten Vidal de Oliveira

AUTOMATIC FAULT DETECTION OF PHOTOVOLTAIC SOLAR GENERATORS APPLYING AERIAL INFRARED THERMOGRAPHY

Esta tese foi julgada adequada para a passagem direta ao doutorado pelo Programa de Pós-Graduação em Engenharia Civil da Universidade Federal de Santa Catarina

Local, x de xxxxx de xxxx.

_____
Prof. Glicério Trichês, Dr. Eng.
Coordenador do Curso

Banca Examinadora:

_____
Prof. Ricardo Rüther, Ph.D.
Orientador
Universidade Federal de Santa Catarina

_____
Dr. Mahammedreza Aghaei
Corientador
University of Freiburg

_____
Prof. xxxx, Dr.
Universidade xxxxxx

“The sun does not wait.”
(Moscardini, 2015)

ABSTRACT

Aerial Infrared Thermography (IRT) is a non-destructive and cost-effective method for detecting faults in large-scale photovoltaic (PV) solar power plants. However, the visual assessment of the images captured by aerial IRT, and the analysis of a large number of image frames is time- and computer-consuming. This doctoral thesis project proposes a method for detecting and classifying faults on PV modules, through aerial IRT images, combining Digital Image Processing (DIP) and Convolutional Neural Networks (CNNs) algorithms. With the preliminary results obtained so far, aerial IRT allowed for the detection of a number of typical PV power plant defects including hot spots, bypassed substrings, short-circuited and open-circuited strings in a 3 MWp R&D PV power plant in Brazil. The IR images acquired were processed with DIP techniques to detect segments of PV modules in the power plant that will be used as samples for training the CNN. The final algorithm is expected to successfully identify faulty PV modules and to classify them by their fault category.

Keywords: Photovoltaic generator fault detection, Aerial Infrared Thermography, Convolutional Neural Networks.

LIST OF ILLUSTRATIONS

Figure 1 - IV curve of a PV module with a bypassed substring in comparison with the IV curve of a healthy module. 24
Figure 2 - EL image of a PV cell with cracks 27
Figure 3 - Fundamental steps in an AVS. 31
Figure 4 - Example of luminance distribution for two different modules: (a) healthy module and a (b) defective module. In the histograms, the green dashed line represents the mean μ and the red pointed line, the upper threshold μ+5σ. 33
Figure 5 - Example architecture of a CNN for a computer vision task (object detection). 35
Figure 6 - Lightweight IRT camera MicroCAM 2 38
Figure 7 - Aerial IRT measurement system used for image acquisition, developed at Fotovoltaica/UFSC using commercially-available UAV and military-grade IR camera. 39
Figure 8 – The 3 MWp R&D PV power plant in Tubarão-Santa Catharina, South of Brazil. 41
Figure 9 - Steps of the Digital Image Processing 42
Figure 10 - Diagram of faults found in the 1 MWp of multi-Si PV modules evaluated in this experiment 47
Figure 11 - Infrared image taken with the Aerial IRT-measurement System showing a disconnected PV module string (intermediate, lighter gray-colored row) 47
Figure 12 - Infrared image taken with the Aerial IRT-measurement System showing a PV module with hot spots in the lower-right edge of the image. 48
Figure 13 - PV module with two visible cracks, caused by the thermal expansion of the corresponding hot spots. 48
Figure 14 - PV module with a number of hot spot cells: image taken with a hand-held infrared camera (FLIR T640), revealing temperature differences in excess of 26 K. 49
Figure 15 - Steps of the preprocessing phase of DIP. (a) Original image (b) Filtered image (c) Contrasted image. 50
Figure 16 - Steps of the segmentation of the images. (a) Preprocessed image (b) Image after Laplacian operator treatment (c) Binary image (d) Binary image with holes filing (e) Border detection (f) Final identification of good quality segments for further analyses. 51
Figure 17 - Example of classification of segments of an image with healthy PV modules (marked with number 4), disconnected PV modules

(marked with number 1) and a PV module with a bypassed substring (marked with number 3). 52
Figure 18 - Example of classification of segments of an image with healthy (marked with number 4) and disconnected (marked with number 1) PV modules 53
Figure 19 - Example of classification of segments of an image with healthy PV modules (marked with number 4) and PV modules with hot spots (marked with number 2). 53
Figure 20 - Example of classification of segments of an image with healthy PV modules (marked with number 4), PV modules with hot spots and soiling (marked with number 2). 54
Figure 21 - Example of luminance distribution for a disconnected PV module 55
Figure 22 - Example of luminance distribution for a PV module with a hot spot 55
Figure 23 - Example of luminance distribution for a PV module with a bypassed substring 56
Figure 24 - Example of luminance distribution for a healthy module .. 56
Figure 25 - Example of segments after augmentation (a) Original segment (b) Horizontal mirrored segment (c) Vertical mirrored segment (d) 180° rotated segment (e) 90° rotated segment (f) 270° rotated segment (g) Croped segment (h) Scaled segment. 57

LIST OF TABLES

Table 1 - Common defects and degradation of PV modules 21
Table 2 - Typical faults found when applying the IEC 61215 and IEC 61646 standards for visual inspection. 23
Table 3 - Examples of thermal abnormalities in PV modules 26
Table 4 - Features of the Aerial IRT-measurement system developed at Fotovoltaica/UFSC using commercially-available UAV and military-grade IR camera. 39
Table 5 - Main features of the 1 MWp multicrystaline PV power block of the 3 MWp R&D PV power plant in Tubarão-Santa Catharina, South of Brazil. 41
Table 6 – Defect classification categories 44

LIST OF ABBREVIATIONS

a-Si – Amorphous Silicon
AI – Artificial Intelligence
AVS – Artificial Vision System
c-Si – Crystalline Silicon
CNN – Convolutional Neural Network
DIP – Digital Image Processing
EL – Electroluminescence
FN – False Negative
FP – False Positive
FPS – Frames per Second
IEC – International Electrotechnical Commission
IRT – Infrared Thermography
m-Si – Monocrystalline Silicon
ML – Machine Learning
NN – Neural Network
O&M – Operation and Maintenance
p-Si – Multicrystalline Silicon
PID – Potential Induced Degradation
PL - Photoluminescence
PV – Photovoltaic
R&D – Research and Development
STC – Standard Test Conditions
TN – True Negative
TP – True Positive
UAV – Unnamed Aerial Vehicle

TABLE OF CONTENTS

1 INTRODUCTION 17
1.1 OBJECTIVES 18
1.1.1 General Objective 18
1.1.2 Specific Objectives 18
2 LITERATURE REVIEW 19
2.1 PHOTOVOLTAIC GENERATION 19
2.2 PV TECHNOLOGIES 19
2.3 COMMON DEFECTS AND FAULTS IN PV MODULES 20
2.4 METHODS FOR DEFECT AND FAULT DETECTION ON PV SYSTEMS 22
2.4.1 Visual Assessment 22
2.4.2 I-V Curve 23
2.4.3 Infrared Thermography (IRT) 24
2.4.4 Electroluminescence (EL) and photoluminescence (PL) imaging techniques 27
2.5 UNMANNED AERIAL VEHICLES 28
2.6 AERIAL IRT 28
2.7 DIGITAL IMAGE PROCESSING (DIP) 30
2.7.1 Image acquisition 31
2.7.2 Preprocessing 31
2.7.3 Segmentation 32
2.7.4 Extraction of Features 32
2.7.5 Recognition and Interpretation 32
2.8 ARTIFICIAL INTELIGENCE (AI) 33
2.8.1 Artificial Neural Networks (ANNs) 34
2.8.1.1 Convolutional Neural Networks (CNNs) 35
2.8.1.2 AlexNet 36
2.8.1.3 Evaluation Metrics 36
3 MATERIALS AND METHODS 38

3.1 IMAGE ACQUISITION 38
3.1.1 Equipment 38
3.1.2 Experimental Site 39
3.2 DIGITAL IMAGE PROCESSING (DIP) 42
3.2.1 Preprocessing 42
3.2.2 Segmentation 43
3.2.3 Classification 43
3.3 AUTOMATIC CLASSIFICATION OF FAULTS 44
4 PRELIMINARY RESULTS 46
4.1 IMAGE ACQUISTION 46
4.1.1 UAV Flight Conditions 46
4.1.2 Faults Detected 46
4.2 DIGITAL IMAGE PROCESSING (DIP) 49
4.2.1 Preprocessing 49
4.2.2 Segmentation 50
4.2.3 Classification 52
5 Expected Results and PRELIMINARY CONCLUSIONS 58
6 WORK PLAN and TIMELINE 59
REFERENCES 61
APPENDIX A – SPREADSHEET FOR THE RECORD OF THE UAV FLIGHT 65

1 INTRODUCTION

On a global scale, renewable energies have led to a shift of paradigm in the electricity sector. Mainly the European countries, some North-American States, and in recent years China have pushed this development, through their progressive energy policy. Today, photovoltaics (PV) is one of the major protagonists of this development, with an installed capacity of over 300 GW in 2017. Recently, PV has also begun to spread in the so called Sunbelt countries like Brazil, where the benchmark of 1 GWp of installed PV capacity was achieved in the end of 2017, and utility-scale PV power plants are building momentum in the Brazilian energy mix. (ABSOLAR, n.d.; IRENA, 2017)

For the integration of this energy source into the electrical power system, and to ensure the PV power generation reliability, operation and maintenance (O&M) of PV power plants is of utmost importance.

Therefore, since the early beginning of utility scale PV power generation, O&M has been adopted as a fundamental method to ensure safety, availability and productivity of PV power plants. During the years, various inspection and fault diagnosis methods have been developed. The most common methods are IV curve tracing, visual inspection, measurement of electrical parameters, electroluminescence (EL) and infrared thermography (IRT). Among these methods, IRT is one of the most popular and reliable fault diagnosis methods (Buerhop et al., 2012), which requires minimum instrumentation, and is carried out without interrupting the operation of PV plants. Furthermore, it can provide information about the exact physical location of a defect, enabling further electrical evaluation, if necessary.

In order to increase the accuracy and speed up the fault detection procedure for megawatt-scale PV power plants or PV systems with limited access like rooftop or façade PV systems, IRT can be combined with aerial inspection techniques. In particular, Unmanned Aerial Vehicles (UAV) are well suited for expanding IRT to large areas in a fast and productive manner (Quater, Grimaccia, Leva, Mussetta, & Aghaei, 2014; Tsanakas & Botsaris, 2012). Aerial inspection by UAV has the advantage of being a contactless, non-destructive and fast inspection method, which can be applied under real-time operation conditions.

However, the visual assessment of the images captured by aerial IRT, and the analysis of a large number of image frames is time- and computer-consuming. A solution to the problem is automated fault detection by combining aerial IRT with computer vision technology, as proposed by many authors (Aghaei et al., 2015; John A. Tsanakas,

Godefroy Vannier, Alexandre Plissonnier, Duy Long Ha, 2016; Kim, Youn, & Kim, 2016, 2017; Rogotis, Ioannidis, Tsolakis, Tzovaras, & Likothanassis, 2014). However, none of the researches succeed in classifying the different types of faults according to their thermic pattern.

A good alternative is to combine Digital Image Processing (DIP) and Artificial Intelligence (AI), to categorize the different types of faults on PV modules. The most popular technique inside AI is Artificial Neural Networks (ANNs), that intend to mimic the way the human brain performs a task of interest (Mayo & Leung, 2018). Between the many different architectures of ANNs, Convolutional Neural Networks (CNNs) have demonstrated clear superiority in visual recognition tasks such as image classification and object detection. (Geng, Zhou, & Cao, 2018) This experiment research proposes a method for detecting and classifying faults on PV modules, through aerial IRT images, combining DIP and CNNs algorithms.

1.1 OBJECTIVES

1.1.1 General Objective

This doctoral thesis project has the main goal of proposing a method for detecting and classifying faults on PV modules, through aerial IRT images, combining DIP and CNNs algorithms.

1.1.2 Specific Objectives

a) Perform aerial IRT inspection of a PV power plant for detecting faults and acquiring IRT images of healthy modules and modules with different faults;
b) Analyze and process the captured IRT images with DIP techniques to detect the modules registered in each image. This will create a dataset of segments of the images classified in categories of possible PV module faults;
c) Train and refine a CNN to classify PV modules between different types of faulty/defective and healthy modules;
d) Obtain a trained CNN capable of successfully classifying PV modules between different types of faulty/defective and healthy modules.

2 LITERATURE REVIEW

2.1 PHOTOVOLTAIC GENERATION

The sun provides all the necessary energy for life on Earth, and it is virtually responsible for the origin of all other sources of energy. Solar energy can be used directly through thermal conversion (solar thermal) or direct electricity generation (photovoltaic conversion of solar energy).

The electrical solar energy conversion can be explained by the photovoltaic effect, which occurs when photons with enough energy and under specific conditions transfer their energy to electrons in a semiconductor material. This method of energy conversion presents great advantages such as its extreme simplicity, the absence of moving parts, its modular characteristic (from mW to MW), the fast installation, the systems high reliability and their low maintenance (Rüther, 2004).

The basic unit of conversion of PV solar energy is the PV cell. The cells are arranged in series in order to constitute a PV module. Similarly, the modules can be connected in series (string) or in parallel to achieve higher current and voltage. The set of elements needed to perform the conversion of solar energy directly into electrical energy is generically called PV system. A system can generate electrical power with suitable characteristics to power electrical machines, such as appliances, lamps, motors and others (Zilles, 2012).

2.2 PV TECHNOLOGIES

Currently there are several PV module technologies. They can be divided into three categories or generations of PV modules (Bagnall & Boreland, 2008; Parida, Iniyan, & Goic, 2011):

a) First generation - Crystalline silicon (c-Si): can be monocrystalline (m-Si) or multicrystalline (p-Si), and is the most widespread technology in the market;
b) Second generation – Thin Films: also uses silicon, but in amorphous form (a-Si), in addition to other materials such as CdTe and CuInGaSe2 or CIGS;
c) Third generation: involves new technologies with high efficiency as organic PV cells, polymer cells, perovskites and heterojunction cells, among others.

In view of the wide variety of technologies, only p-Si has been evaluated in this thesis, since it is the most commercially available. For p-Si, the most common module configuration uses 60 or 72 cells,

typically connected in series. These cells are connected into strips and encapsulated in order to protect them from the environment, and provide mechanical resistance to the PV module.

At the back of the modules there is usually a connection box, where the connections of the cells in series and the bypass diodes are kept. The bypass diodes provide an alternative path for the current when part of the module is shaded, in order to avoid "hot spots". This reduces the loss of energy and the risk of irreversible damage to the affected cells (Zilles, 2012).

2.3 COMMON DEFECTS AND FAULTS IN PV MODULES

A fault is defined as anything that might decrease the PV module performance or change its characteristics. On the other hand, a defect is an unexpected thing that was not observed before on the module, and does not necessarily imply power loss.

Table 1 summarizes defects that are commonly found on PV systems. This research will focus on faults that cause disconnected modules, “hot-spots” and bypass diode problems.

Table 1 - Common defects and degradation of PV modules

Faults found in all PV modules		
Defect	**Possible Reason**	**Effect on PV module**
Delamination	Problem of adhesion between the glass, encapsulant, active layers and back layers, caused by contamination or environmental factors	Humidity ingress, corrosion, reduced module performance, isolation fault
Back sheet adhesion loss	Mechanical stress, UV-radiation, heat, humidity	Corrosion, mechanical stress, risk of electric arcs
Junction box failure	Poor fixing, poor manufacturing, bad wiring	Higher resistance, risk of thermal damage
Faults found in silicon wafer-based PV modules		
Defect	**Possible Reason**	**Effect on PV module**
EVA discoloration	UV-radiation; humidity; temperature	Higher light absorption in polymer, reduced module performance
Cell cracks	Mechanical stress induced by mechanical or thermal loads	Insulated cell areas, reduced module performance
Snail trails	Grey/black discoloration of the silver paste of the front metallization of solar cells	Higher resistance, insulated cell areas, reduced module performance
Burn marks	Solder bond failure, ribbon breakage, thermal fatigue	
Potential Induced Degradation (PID)	Migration of ions from the front glass through the encapsulant to the anti-reflective coating at the cell surface driven by the leakage current in the cell to ground circuit.	"Hot-spots", low shunt resistance, module delamination, reduced module performance
Disconnected cell or string interconnect ribbons	Problems in production process, mechanical stress, thermal stress	Bypass diode activation, reduced module performance, "hot-spots", glass breakage
Defective bypass diode	High voltage discharges and mechanical stress	"Hot-spots", back sheet burns
Broken glass	Previous glass damage, mechanical load, thermal stress	Corrosion, loss of mechanical stability, cell breakage
Faults found in PV systems		
Defect	**Possible Reason**	**Effect on PV module**
Connector insulation failure	Pinched wire	Short circuit/no power output
Wiring failure	Repeated flexing of wire, faulty cabling, crack bar ruptures on cables, insulation failure, extreme weather conditions	Open circuit, short circuit, no output power, safety problem, fire
Connector overloading	Wiring undersizing	Overloading
Soiling or shading	Accumulation of dust and soil	Reduction in energy output, "hot-spots"

Source: Adapted from (Aghaei, 2016; Köntges et al., 2014; Renganathan, Natarajan, & Jahaagirdar, 2016)

2.4 METHODS FOR DEFECT AND FAULT DETECTION ON PV SYSTEMS

With a more widespread adoption of the PV technology, the importance of O&M of power plants increases. Investigation of novel monitoring methods is a critical issue for the solar energy market growth. With the advance of data analytics, sensors and artificial intelligence, one applied solution is a system supervisory platform. But, these systems normally measure power, current and voltage of each string, making it hard to detect faults that affect only one module. They also cannot detect non-energy, latent risk factors, as hot-spots or sub-string failures, that do not reduce power production in the short-term, but can cause damage to the system in the long run (Andrews, 2018). Therefore, onsite inspections are still necessary.

The most traditional diagnosis tools to detect defects and failures on PV systems are: visual inspection, I-V curve measurements, and infrared thermography analyses. Recently new methods have been gaining attention because of their lower cost, like for instance electroluminescence (EL). The following subsections describe some of these methods.

2.4.1 Visual Assessment

Visual inspection is the first step, and also the quickest and most effective evaluation tool/technique. Visual inspection can detect yellowing/browning, delamination, bubbles, cell cracks, misalignments, bad connections, and burnt cells. The complete list of typical faults found by visual inspection, according to the IEC 61215 and IEC 61646 standards, is presented in Table 2. For the assessment, the standards require more than 1000 lux of natural illumination (Köntges et al., 2014; Munoz, Alonso-García, Vela, & Chenlo, 2011).

Table 2 - Typical faults found when applying the IEC 61215 and IEC 61646 standards for visual inspection.

PV module component	PV module failures
Front of PV module	Bubbles, delamination, yellowing, browning.
PV Cells	Broken cell, cracked cell, discolored anti-reflection.
Cell metallization	Burned, oxidized
Frame	Bend, broken, scratched, misaligned.
Back of module	Delaminated, bubbles, yellowing, scratches, burned.
Junction box	Loose, oxidation, corrosion.
Wires/connector	Detached, brittle, exposed electrical part.

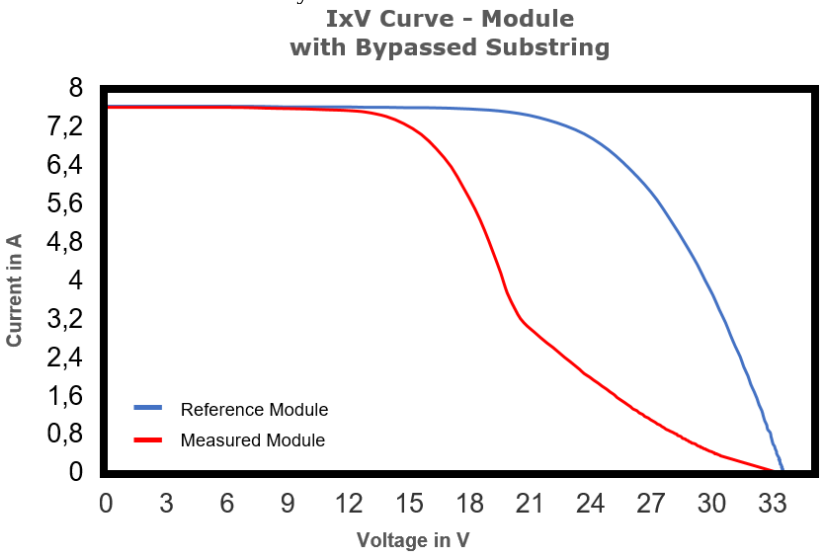
Source: (Köntges et al., 2014)

2.4.2 I-V Curve

Historically, I-V curve tracing or electrical inspections are the main method for PV performance analysis. They determine short-circuit current, open-circuit voltage, fill factor, maximum power point and other parameters. As the reduction of power production is the main evidence of a problem, an I-V measurement curve gives sufficient information about the PV module condition. Figure 1 presents the I-V curve of a module with a bypassed substring. The performance of the faulty module is reduced by 35.8%, in comparison to a neighboring healthy module (reference module).

Normally, I-V curves are measured with solar simulators under standard test conditions (STC – Cell junction temperature = 25°C, Irradiance=1000 W/m², the spectral distribution of irradiance Air Mass=1.5). They can also be performed under real sunlight exposure, where the PV modules do not meet the STC during the test measurement, with measurements corrected for STC. Usually the radiation is less than 1000 W/m², the cell junction temperature is higher than 25°C, and Air Mass is hardly ever 1.5. The measured curves can be corrected to STC and can be used as an ideal reference for comparison of different PV modules (Aghaei, 2016; Köntges et al., 2014; Munoz et al., 2011).

Figure 1 - IV curve of a PV module with a bypassed substring in comparison with the IV curve of a healthy module.



In power plants, these inspections can be performed by an I-V curve tracer on all or a subset of strings on a site. As the method is expensive and labor intensive to be applied to an entire site, a typical power plan has 25% or less of its strings verified per measurement campaign. This means that many defects are ignored. The inspection also requires the opening of the fuse circuit, leading to a higher likelihood of a fuse failure (Andrews, 2018).

For I-V characteristic measurements, there are many aspects affecting measurement accuracy, as calibration of sensors, varying meteorological conditions during inspection, variable soiling of modules, module mismatch and inter-string temperature variations.

2.4.3Infrared Thermography (IRT)

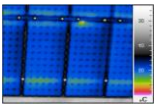
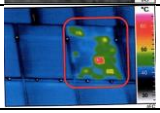
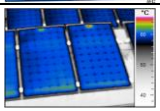
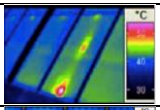
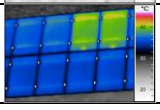
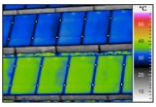
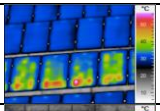
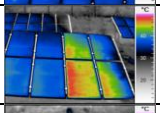
Infrared thermography (IRT) measures the radiation emitted by the surface of any body in the infrared wavelength spectrum between 1.4 – 15µm. The infrared thermography employed for PV applications usually detects wavelengths in the mid-infrared wavelength range of 7 – 14 µm, which is an equilibrium between costs, availability and measuring conditions of IRT sensors (Tsanakas et al. 2013).

As in a PV plant all PV modules receive in principle the same amount of irradiance, the modules or cells that are not converting photons into electricity, will convert them into heat. Therefore, energy losses will appear in IRT images as temperature differences.

IRT can be used for the detection of a great number of defects in PV cells, modules and strings, since the majority of the defects have an impact on the cell thermal behavior. Such thermal patterns have been identified and classified in previous studies (Buerhop et al. 2007, Buerhop et al. 2012, Köntges et al. 2014) and are now standardized in the international standard IEC TS 62446-3 Edition 1.0 2017-06, as shown in Table 3. On the table, it is visible the resemblance of faults numbers 1, 2 and 3. Therefore, they are not differentiated in this work, being referenced as “hot-spots”.

IRT is a non-destructive and contactless method that can be performed under steady-state operation conditions. Furthermore, IRT can provide information about the exact physical location of an occurring fault, which allows for posterior electrical diagnosis of the problem. Buerhop et al. (2012) have proven that IRT is a reliable fault diagnosis method, which requires a minimum of instrumentation and can be applied without interrupting the operation of the PV plant.

Table 3 - Examples of thermal abnormalities in PV modules

Examples of thermal abnormalities in PV modules				
N.	**Thermogram**	**Description**	**ΔT (K)**	**Recommendation**
1		Suspicious conductor strip	>3 K	• In-depth visible check; • Evaluation by a level 2 certified thermographer based on detailed high-resolution backside thermogram/photo.
2		Overheated cell	>20 K	• Check for shading or soiling effect; • Replace the module.
3		Module with broken front glass	0 K to 7 K	• Replace the module.
4		Heated module junction box	>3 K higher temperature compared to nearby junction box	• Personal review by a PV expert or termographer level 2.
5		Substring in short circuit	Averaged 2 K to 7 K higher than substring	• Check module and bypass diodes for proper function under reverse biasing
6		Bypassed substring (open circuited)	2 K to 7 K	• Replace the module.
7		Several substrings bypassed	2 K to 7 K	• Replace the module.
8		Modules in open circuit	2 K to 7 K	• Check module; • Check state of operation of inverter; • Check condition of cabling, connectors and fuses.
9		Modules in short circuit	2 K to 7 K	• Check module; • Check cabling.
10		Polarity of connector reversed	3 K to 12 K	• Check polarity of modules connectors; • Check polarity of string connectors.
11		Single cell is partly shaded (not a defect)	20 K to 70 K	• Remove object that is causing the shadow.

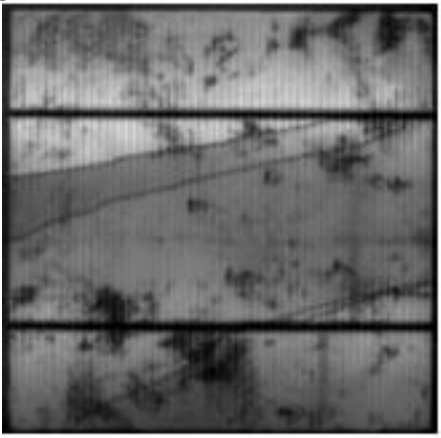
Source: Adapted from (International Electrotechnical Commission (IEC), 2017; VATh, 2016; Weinreich, Haas, Zehner, & Becker, 2011)

2.4.4 Electroluminescence (EL) and photoluminescence (PL) imaging techniques

Electroluminescence (EL) and photoluminescence (PL) characterization are non-invasive methods for the detection of cell and module defects at any stage in the lifetime of a PV module. These techniques provide local information about shunts, contact and series resistances, microcracks and snail trails, inactive cell areas, inhomogeneity of materials and potential induced degradation (Kropp, Berner, Stoicescu, & Werner, 2017).

Electroluminescence is obtained from photons emitted by the radiative recombination of charge carriers excited under forward bias. Typically, an external power supply electrically stimulates the module under investigation to emit the electroluminescent radiation. For c-Si, the radiation ranges in the near-infrared at wavelengths around 1150 nm. Cell defects locally reduce or prevent the emission of EL radiation, and are thus revealed and visualized as black areas by cameras that are sensitive to these wavelengths. Usually, such measurements are carried out in the dark (Djordjevic, Parlevliet, & Jennings, 2014; Frazão, Silva, Lobato, & Serra, 2017; Kropp et al., 2017; Munoz et al., 2011). Figure 2 shows an EL image of a PV cell presenting some cracks that are not affecting the current flow over the cell at the present stage, but which might evolve into active defects.

Figure 2 - EL image of a PV cell with cracks



Source: (Köntges et al., 2014)

The excitation can also be obtained by means of radiation incident over the solar cell, in which case the light obtained is due to the PL effect (Munoz et al., 2011).

2.5 UNMANNED AERIAL VEHICLES

Unnamed Aerial Vehicles (UAVs) are aircrafts capable of being operated remotely or autonomously. They were first developed for military applications, but the recent developments in the field of UAV made this technology available for civil activities like disaster relief, energy equipment and power line monitoring, environmental control, forest inspection and mine monitoring, among others (Aghaei et al., 2015). Especially in the energy and agriculture sectors, UAVs are becoming more popular due to their advantage of area coverage, precise imagery, fast detection, high flexibility, light weight, low cost and ability to operate in hostile environments (Grimaccia, Aghaei, Mussetta, Leva, & Quater, 2015; Tsanakas & Botsaris, 2012).

The expansion of the UAVs use depends on their ability of moving autonomously and safely in diverse environments and legal issues. The legal requirement of a certified operator in a vision camp of each UAV is an obstacle in the UAV law that stands worldwide and also in the law of Brazil.

2.6 AERIAL IRT

Traditionally, IRT inspections for PV applications are performed with handheld IRT cameras on the ground or on lifting platforms to increase the coverage. This procedure is dependent on human labor and competence and it is very time-consuming and labor intensive. As a result, the monitoring accuracy is prone to human error and the uncertainty of the method amplified. In order to increase the cost-effectiveness and employ IRT for large-scale PV plants or roof-mounted PV systems with limited access, IRT can be combined with aerial technologies like UAV.

Currently, this method is attracting attention. There is still a lot of potential in applying this inspection method for PV plants, which can revolutionize the future of PV plant monitoring procedures (Aghaei et al., 2015), especially when combining it with automation technologies, like automated route planning and automatic defect identification.

Aerial IRT is performed by visual and IR sensors that are mounted on the UAV platform. It provides real-time and precise imagery in a time-

efficient manner. Detectable defects and failures are cracks, corrosion, broken parts, hot-spots, snail trails, discoloration, dirty points, open-circuited modules or strings and potential induced degradation (Quater et al., 2014; Tsanakas & Botsaris, 2012). Depending on the mission and planned direction, UAV can fly at different altitudes to identify specific defects or faults (Leva, Aghaei, & Grimaccia, 2015).

The aerial IRT process is held in three stages: acquisition, analytics and remediation (Andrews, 2018). For the acquisition step, the UAV has to fly a designated rote making successive scans over the site to build an imagery database covering all modules in the system. As the equipment has a limited battery time, each flight has a duration of around 20 minutes. The capture rate for a standard resolution is around 10 MW/day, but the UAV can cover more than 40 MW/day at a lower image resolution and higher altitudes.

During the flight, various environmental stress factors like weather conditions, air turbulence and sunlight reflection may affect the measurements and consequently the quality of the aerial IRT images. In addition, self-shading, high velocity of the UAV, drift and crab during the flight and an oblique orientation angle of the IRT sensor should be avoided.

The optimum conditions for aerial IRT monitoring can be summarized as follows (Aghaei, Leva, Grimaccia, & Milano, 2016; Leva et al., 2015; Quater et al., 2014):

a) The angle of the IRT sensor mounted on UAV should be oriented as perpendicular toward the PV modules, and should be kept constant;
b) The minimum flight altitude should be five meters in order to avoid any self-shading of the UAV during the inspection;
c) The aerial IRT should be performed on cloudless, sunny and clear days. In addition, the wind speed should not exceed 4 m/s, because higher wind speeds can cause air turbulences and shake the UAV during the inspection procedure;
d) The best time for aerial IRT by UAV is around noon and before afternoon when the position of the sun is more perpendicular on PV plants. Furthermore, the irradiance should be more than 600 W/m2 on the plane of the PV array under inspection. Nevertheless, it depends on the geographical location of PV plant hence it can be performed at various times since the position of the sun differs in the Northern or Southern hemisphere;

e) The direction of the flight should be planned before each inspection mission in order to avoid any drift and crab during the aerial IRT monitoring.

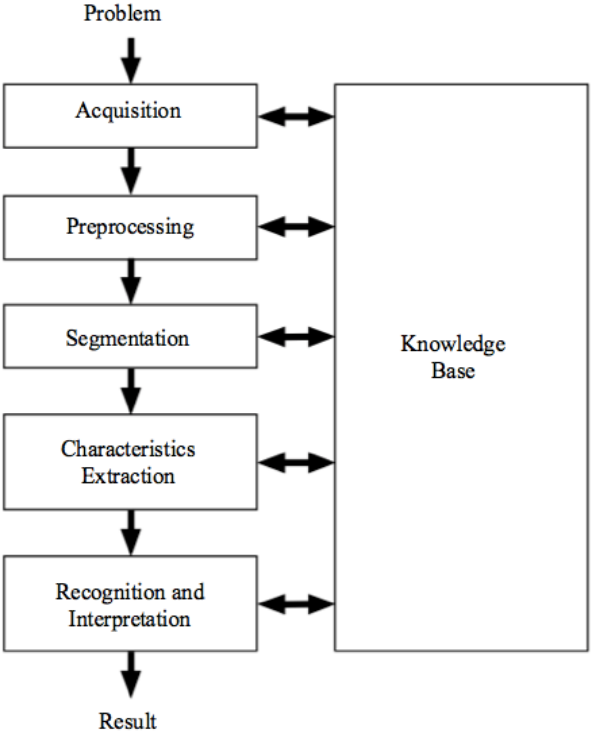
The acquired data is then analyzed and an actionable report is produced. With a detailed site mapping, it is possible to have an accurate location of the system faults and the remediation can be planned based on full knowledge of the site state. The report is passed to the stakeholders for remediation actions as review of connection, replacement of modules and others.

2.7 DIGITAL IMAGE PROCESSING (DIP)

The area of digital image processing (DIP) has been an object of increasing interest, because it allows a large number of applications applying the processing of image data for storage, transmission, and representation for autonomous machine perception. (Gonzalez & Woods, 2002)

An Artificial Vision System (AVS) is a computerized system capable of acquiring, processing and interpreting images corresponding to real scenes. Figure 3 presents schematically a block diagram of an AVS. Its main steps are explained below. (Filho & Neto, 1999)

Figure 3 - Fundamental steps in an AVS.



Source: Adapted from (Filho & Neto, 1999).

2.7.1 Image acquisition

The acquisition step converts an image into an appropriate numeric representation. This requires a physical device sensitive to a range of energy in the electromagnetic spectrum and a digitizer device, which converts the analog electrical signal into digital information (Filho & Neto, 1999; Gonzalez & Woods, 2002).

2.7.2 Preprocessing

The function of the preprocessing step is to improve the image quality for subsequent steps, removing imperfections such as: presence of noisy pixels, improper contrast or brightness, interrupted or improperly connected characters (Filho & Neto, 1999; Gonzalez & Woods, 2002).

2.7.3 Segmentation

The segmentation step consists of dividing an image into its constituent parts or objects and is based on the principle that different sections of a digital image have different pixel values. This task, although simple to describe, is one of the most difficult to implement. In general, the more accurate the segmentation, the more likely the recognition is to succeed. One of the basic methods for region segmentation in image processing is transforming the image to binary information. Parts of images can be separated into white and black completely. It distinguishes the image to 0 and 1 divisions based on a threshold. A reasonable threshold is the key to determine a more satisfactory segmentation (Aghaei et al., 2015; Zhang, Wu, Yang, Jiang, & Zhou, 2017).

2.7.4 Extraction of Features

As conventional ML techniques cannot process natural data in their raw form, it is important extract characteristics of the images resulting from the segmentation through descriptors that allow to characterize each segment accurately. These characteristics could be the pixel's values or the maxima and minima intensity of an image, for example (Filho & Neto, 1999; Lecun, Bengio, & Hinton, 2015).

With the rise of CNNs, this process is not necessary, since the hidden convolutional layers do a similar job to the feature extractors previously used. The algorithm is fed with original raw data and it discover the features needed for the classification (Lecun et al., 2015). More information regarding ML and CNNs is presented in section 2.8.

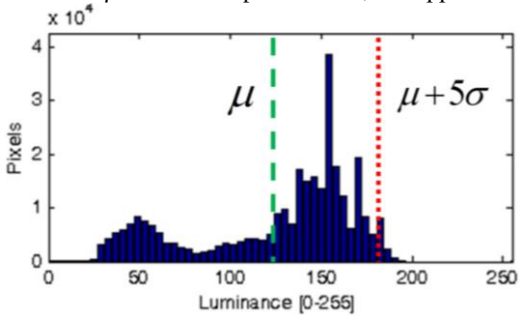
2.7.5 Recognition and Interpretation

Recognition is the process of assigning a label to an object based on its characteristics, translated by its descriptors. The task of interpretation, on the other hand, is to assign meaning to a set of recognized objects (Filho & Neto, 1999; Gonzalez & Woods, 2002).

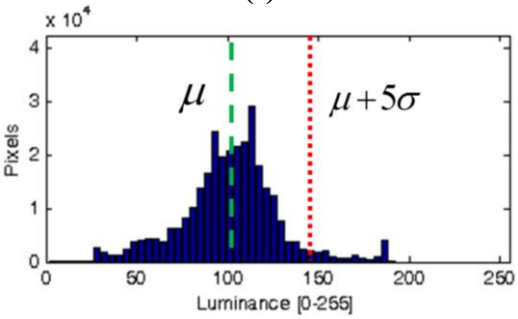
In Aghaei et al., (2015), a novel method was proposed for the detection of faults in PV modules based on the luminance distribution of the infrared images. Figure 4 shows an example of the luminance distribution difference between a healthy module and a defective module. For defective modules, the distributions present *fat tails* for luminance larger than 5σ over the average. That shows that with a simple analysis of

the segments, it is possible to have a more accurate decision on the defect categorization.

Figure 4 - Example of luminance distribution for two different modules: (a) healthy module and a (b) defective module. In the histograms, the green dashed line represents the mean μ and the red pointed line, the upper threshold μ+5σ.



(a)



(b)

Source: (Aghaei et al., 2015)

2.8 ARTIFICIAL INTELIGENCE (AI)

Artificial intelligence (AI) is the science of engineering intelligent machines and computer programs. In traditional computer programming, this engineering happens with written code that details every step the program will take. But with the rise of machine learning (ML), a program can learn and improve from experience without being explicitly programmed. (Mayo & Leung, 2018)

Inside ML, there are many algorithms that can be used, like *Naïve Bayes*, Support Vector Machine, Genetic Algorithm and Decision Tree. The most popular technique is inspired by the structure and function of

the human brain and is called artificial neural networks (ANNs). They are commonly used because they can deal with highly nonlinear systems and allow constant updates in the model. (Mayo & Leung, 2018)

2.8.1 Artificial Neural Networks (ANNs)

Artificial Neural Networks (ANNs) are a type of learning algorithm that attempt to mimic the way the human brain performs a task of interest (e.g., classification, detection, filtering). They are composed of a set of simple, connected processors called neurons, each producing a sequence of real-valued activations. The fundamental property of an ANN is its ability to learn from the environment (read set of examples), through an iterative process of adjustments applied to synaptic weights and bias levels. Learning an assignment is about finding weights that make the ANN exhibit a desired behavior, such as driving a car. Depending on the problem and how the neurons are connected, such behavior may require long causal chains of computational stages, where each stage transforms the aggregate activation of the network. Deep Learning is about accurately assigning credit across many such stages. (Junior, 2011; The, Ai, Dalle, & Galleria, 2014)

The algorithms of neural networks are characterized mainly by the learning rule employed and its structure (architecture). As for the architecture there are as main variations the number of layers used, if all the neurons of a layer are connect or not to all of the next one, and if there are recurring connections or not. According to the applied learning method, certain learning tasks are possible for the ANN in question.

In general, the learning methods are framed in two paradigms, the learning with or without a teacher. In learning with a teacher (supervised learning) it is considered that for a given set of examples presented during a training step of the neural network, the teacher who has knowledge about the environment (input data) determines which ideal output to be presented by the neural network. From the difference between the ideal (desired output) and the output presented by the network, the free weights of the network are updated, and learning takes place. One of the learning models without a teacher is unsupervised (or self-organized) learning. In this paradigm there is no external reference to the network as to the correct or incorrect classification, and an independent measurement of the task is provided to adjust the weights. (Canena & Ângeluz da Costa, 2012)

2.8.1.1 Convolutional Neural Networks (CNNs)

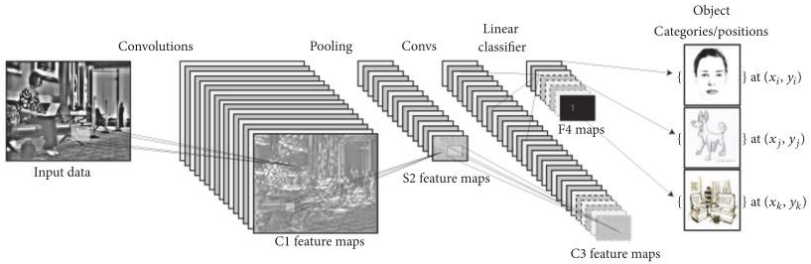
Convolutional Neural Networks (CNNs) were inspired by the visual system's structure and are the state-of-the-art method for image classification (Kamilaris & Prenafeta-Boldú, 2018; Malof, Bradbury, Collins, & Newell, 2016; Mehta, Azad, Chemmengath, Raykar, & Kalyanraman, 2017; Voulodimos, Doulamis, Doulamis, & Protopapadakis, 2018). They are easy to train when there is a huge amount of labeled images that represent the different categories.

CNNs are layered sequences and each has a specific function in the propagation of the input signal. There are three main types of neural layers, namely, (i) convolutional layers, (ii) pooling layers, and (iii) fully connected layers. Figure 5 illustrates the CNN architecture for an object detection in image task and its three main layers:

a) Convolutional layers: responsible for extracting attributes from the input volumes.
b) Pooling layers: in charge of reducing the spatial dimensions of the input volume after the convolutional layers, reducing the computational work of the network.
c) Fully-connected layers: responsible for the final classification of the images, like a conventional neural network.

In the end, the CNN output is the probability that the input image belongs to one of the classes for which the network was trained. (Carneiro & Silva, 2017)

Figure 5 - Example architecture of a CNN for a computer vision task (object detection).



Source: (Voulodimos et al., 2018)

2.8.1.2AlexNet

AlexNet is a type of CNN architecture created in 2012 that has inspired several other CNNs. It has five convolutional layers, max-pooling layers and three fully connected layers with dropout. Max-pooling layers are pooling layers that subsample data, applying overlapping; therefore they create redundancy and decrease the error of the network. Dropout is a technique that removes, randomly, at each iteration of training, a percentage of the neurons of a layer, returning it at the next iteration. It allows the ANN to learn stronger features, since the neurons cannot depend on the presence of each other. (Krizhevsky, Sutskever, & Hinton, 2012)

The ANN was applied to classify images in 1000 categories. It won the ILSVRC 2012 (ImageNet Large Scale Visual Recognition Challenge), which is the most famous computer vision competition of the world (Carneiro & Silva, 2017).

2.8.1.3 Evaluation Metrics

Performance indices quantify the capacity of the ANN in identifying the events of interest. The evaluation and comparison of the performance of ANNs in the identification of events have used the indexes of precision, sensitivity and efficiency. (Junior, 2011)

Since the problem consists of multiple classes, it is necessary to extend the definitions of positive and negative examples by testing each class against all others. Thus the interest class is defined as the positive class while all others are defined as negative. The following result possibilities are obtained (Carneiro & Silva, 2017):

a) True Positive (TP): Segments correctly classified as the class of interest.
b) True Negative (TN): Segments correctly classified as not being the class of interest.
c) False Positive (FP): Segments incorrectly classified as the interest class.
d) False Negative (FN): Segments incorrectly classified as not being the class of interest.

The number of TPs, TNs, FPs and FNs are used to calculate the metrics of the results in the following equations. The first metric, precision, is defined in Equation 1.

$$\text{Precision} = \frac{TP}{TP+FP} \quad (1)$$

This index provides the proportion of all segments that were identified in one class that in fact belong to this class. That is relevant because false identifications cause unnecessary human work, as for example, to check faults that actually do not exist.

The sensibility measures how well the ANN is able to identify each class among the segments and is presented Equation 2.

$$\text{Sensibility} = \frac{TP}{TP+FN} \quad (2)$$

A good ANN should have high precision and high sensibility for all the classes. Efficiency is an index that expresses the relationship between sensitivity and specificity indices in only one measure. It is described in Equation 3.

$$\text{Efficiency} = \frac{TP+TN}{TP+TN+FP+FN} \quad (3)$$

3 MATERIALS AND METHODS

3.1 IMAGE ACQUISITION

3.1.1 Equipment

For the image acquisition, an Aerial IRT-measurement system was developed applying the UAV DJI Phantom 3 Advanced model. It was modified and equipped with a lightweight infrared camera (Figure 6) and a video transmission system, as presented in Figure 7. The main features of the IRT-measurement system are given in Table 4.

For the correct classification of faults in the PV modules, in addition to the aerial IRT measurements, infrared images of a selected specimen with a handheld IR camera, FLIR T640, were taken. This was necessary to quantify the detected temperature differences, since the IRT system could not provide radiometric data. The IR camera featured a 640 x 480 uncooled microbolometer with a spectral range of 7.8 – 14 µm.

Figure 6 - Lightweight IRT camera MicroCAM 2



Source: (Thermoteknix, 2018)

Figure 7 - Aerial IRT measurement system used for image acquisition, developed at Fotovoltaica/UFSC using commercially-available UAV and military-grade IR camera.



Table 4 - Features of the Aerial IRT-measurement system developed at Fotovoltaica/UFSC using commercially-available UAV and military-grade IR camera.

UAV features		**IR camera specifications**		**Video Transmission System**	
Weight	1,280 g	**Sensitivity**	< 60 mK	**Signal**	Analogic video signal
Flight height	6,000 m	**Spectral range**	7 – 17 µm	**Transmitter**	BosCam Transmitter
Flight velocity	max. 16 m/s	**Pixel pitch**	17 µm (640x480)	**Antenna**	Cloverleaf 5.8 GHz
Flight time	13 min.	**Pixel count Frame rate**	307,200/ 30 FPS	**Transmission power**	1W
Flight range	3.5 km	**Weight**	80 g	**Transmission frequency**	5.8 GHz

Source: (Thermoteknix, 2018)

3.1.2 Experimental Site

The images were taken at the 3 MWp R&D PV power plant Cidade Azul, located in the city of Tubarão (latitude 28°28’ south, longitude 49°0’ west) in the state of Santa Catharina, in South Brazil. The PV plant, as seen in Figure 8, consists of three 1 MWp-blocks of different PV technologies – namely multicrystalline PV modules at the top of the picture, followed by thin-film CIGS (Cupper Indium Gallium Selenide)

in the middle, and thin-film amorphous silicon modules at the bottom of the picture.

In the end of 2016, a meteorological tsunami hit the region where the plant is located. During this phenomenon, wind gusts, measured by a wind tower next to the plant, reached 210 km/h. The maximum average of one-second measurements of wind speed for ten continuous minutes was 112 km/h. This extreme climatic event has created great havoc and caused damages to the solar PV power plant. However, only 0.1% (20) of the PV modules were detached from their ground-mounted metal structures. Moreover, several PV module strings had their electrical wiring severed by the strong winds.

The images shown in this thesis were taken after the incident, to analyze the overall condition of the 1 MW block of multicrystalline PV modules. The experiment was focused on the multicrystalline PV block of the power plant, since this technology operates with higher currents, facilitating the task of detecting faults according to temperature differences. The features of the analyzed part of the PV plant are presented in Table 5. The PV modules are fixed on ground mounted racks that support three rows of twenty portrait-oriented modules with an inclination of 30°, facing true North. As the PV plant is part of a R&D project, different inverter topologies have been adopted to test the effect of different inverter concepts and loading on the PV system performance in this climate region.

Figure 8 – The 3 MWp R&D PV power plant in Tubarão-Santa Catharina, South of Brazil.



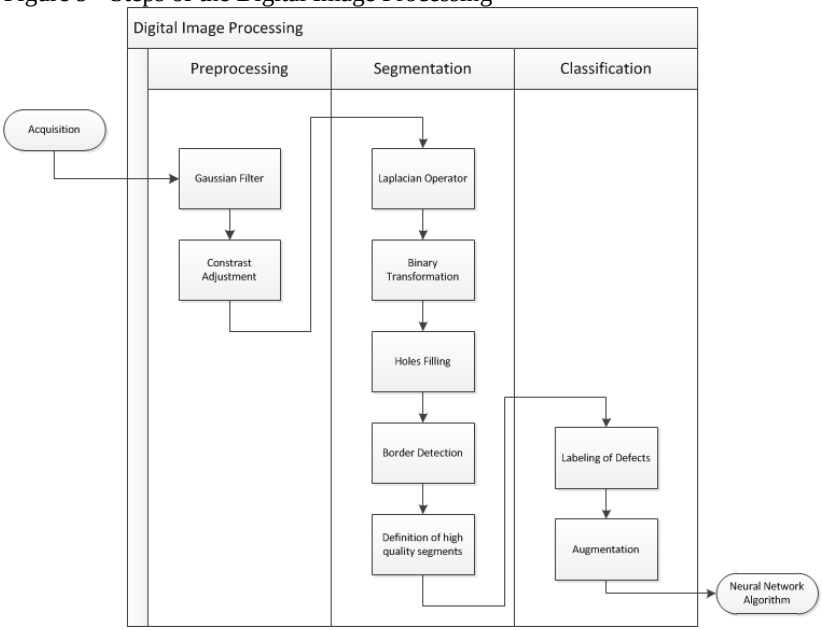
Table 5 - Main features of the 1 MWp multicrystaline PV power block of the 3 MWp R&D PV power plant in Tubarão-Santa Catharina, South of Brazil.

Power plant data	**Subsystem size (kWp)**	**Number of Modules**	**Number of Strings**	**Inverter size/ model**
Installation year: 2014 Operation period: 3 years Module: Multicrystalline Yingli Solar YL 245C.29b	216.34	883	56	18 x 10 kW ABB PVI-10.0-TL-OUTD
	111.72	456	24	4 x 27.6 kW ABB TRIO-27.6-TL
	53.90	220	10	55 kW ABB PVI-55
	.161.70	660	30	165 kW ABB PVI-165.0
	485.10	1.980	99	500 kW ABB PVS800-57-0.500kW-A
Total	1,028.76	4.199		

3.2 DIGITAL IMAGE PROCESSING (DIP)

Based on Figure 3, the method of DIP applied on the acquired images is presented in Figure 9. It is important to notice that, as described in 2.7.4, the step of features extraction is not necessary, since CNNs are being used. Each step of the method is described in the following subsections. All steps of DIP were carried out with filters and functions available at the MATLAB® environment.

Figure 9 - Steps of the Digital Image Processing



3.2.1 Preprocessing

The acquired pictures are already in grayscale, which are clearer than colored images. In grayscale pictures, each picture is in the interval range [0; 255], 0 for black and 255 for white areas, thus the luminance of a pixel is usually described by one single byte, which corresponds to one of 256 levels. The first step of preprocessing is filtering, in order to eliminate noise effects, despite causing blurred vision on the edge of the image. A Gaussian filter is chosen, because besides decreasing noises, it can highlight the boundaries of PV modules, facilitating the segmentation

part (Aghaei et al., 2015). At the end of the phase, the contrast is also adjusted, in order to highlight the PV modules borders to prepare for the next step.

3.2.2 Segmentation

The segmentation part is facilitated by the Laplacian (gradient) operator, defined by Equation 4.

$$\nabla^2 f(x,y) = \frac{\partial^2 f}{\partial x^2} + \frac{\partial^2 f}{\partial y^2} \quad (4)$$

It highlights gray level discontinuities in an image and deemphasizes slowly varying gray level changes. It is useful in the process of borders detection, making the border of PV modules more visible. But the operator is very sensible to noise, therefore the need of a previous filter (Filho & Neto, 1999).

The next step is to transform the image to binary, using a threshold chosen by numerous trials, in order to detect each PV module of a picture. They also pass through a hole filling process, when possible holes are excluded, making the image clearer. The segments are then filtered by size, in order to suppress small segments or segments of the ground.

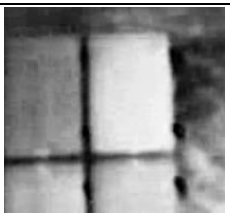
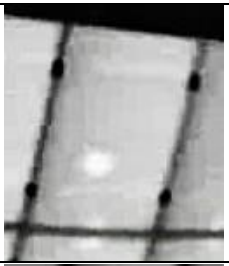
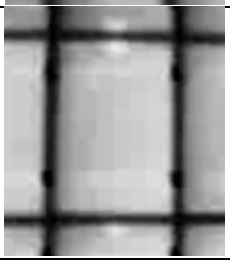
3.2.3 Classification

Based on (VATh, 2016), the segments of PV modules are categorized according to their thermic pattern. They are classified in four categories, as shown in Table 6 which is based on Table 3. The short-circuited modules are not considered in this analysis, because their thermic pattern can be very similar to PV modules with hot spots. Therefore, they are not easily distinguished and could make the automatic classification process harder.

After the labeling, the luminance distribution of each segment is calculated in order to compare and find a pattern for each category.

As the dataset obtained is not large, data augmentation techniques are implemented. This processing artificially enlarges the number of segments, helping to improve the overall learning procedure and performance, feeding the model with varied data. (Kamilaris & Prenafeta-Boldú, 2018) Transformations are label-preserving, and included rotations, dataset segments cropping and scaling, transposing and mirroring.

Table 6 – Defect classification categories

Category	Description	Thermic Pattern
1	Disconnected module	
2	Module with one or more hot spots	
3	Module with a bypassed substring	
4	Healthy module	

3.3 AUTOMATIC CLASSIFICATION OF FAULTS

The employed architecture of the CNN is initially based on quantity and types of layers of AlexNet. After multiple iterations, there will be addition or removal of layers in order to improve the classification and the computational time.

The training of the network will be divided in two datasets. The first one will use balanced quantity of samples for each category. It will

be limited by the number of segments available of category of fault number 3 (bypassed substring), since it has the lower quantity of samples. The second one will not have balanced categories, so it will probably perform better in the detection of the category with more samples (number 4, healthy modules).

In both datasets, 70% of the samples will be used for training, 10% for validation and 20% for testing, following the same proportion for each class. The final values of the parameters used in this training will be adjusted after empirical attempts at combinations, using as evaluation methods the precision, sensibility and efficiency of each one of them.

4 PRELIMINARY RESULTS

This section presents the preliminary results obtained so far.

4.1 IMAGE ACQUISTION

4.1.1 UAV Flight Conditions

Measurements were carried out under sunny weather conditions, clear sky with 2/8 cloud coverage, wind speeds of 3 m/s and irradiances above 800 W/m2, measured on the PV array plane. A flight height of 5 m was adopted in order to avoid self-shading, and the angle of the camera was kept perpendicular to the PV modules (Aghaei et al., 2015). For the control of the flight conditions, a worksheet for the record of the flight was developed and applied, as seen in Appendix A.

Flights were performed by a trained pilot, respecting the local UAV laws. The route was programmed through a smartphone application, so that the flight would be steady and the quality of the images as good as possible.

4.1.2 Faults Detected

The Aerial IRT-measurement system was able to detect multiple faults on the multicrystalline silicon (p-Si) PV modules. They are presented in different colors in Figure 10. The two blue dots correspond to activated bypass diodes and the 15 green squares are modules with hot spots. These thermal patterns can indicate modules that are damaged, with broken cells, or that are likely to degrade rapidly.

In addition to the modules with defects, the images also showed whole strings with anomalies: the red lines in Figure 10 represent disconnected strings and orange areas indicate shorted-circuited strings. These problems can be caused by blown fuses, bad connections between modules and between strings, or even damaged modules inside the strings. Figure 11 and Figure 12 present some of the images acquired with the aerial IRT-measurement system, showing respectively a disconnected string and a module with hot spots. For the further accurate labeling of images, the temperature deviations were confirmed with the handheld infrared camera. Most of the modules found with hot spots had their glass shattered, probably by thermal expansion. An example of it is the module shown in Figure 13, which presented hot spot temperatures 26 K higher

than the rest of the module, as seen in Figure 14, explaining the crack caused by thermal expansion.

Figure 10 - Diagram of faults found in the 1 MWp of multi-Si PV modules evaluated in this experiment

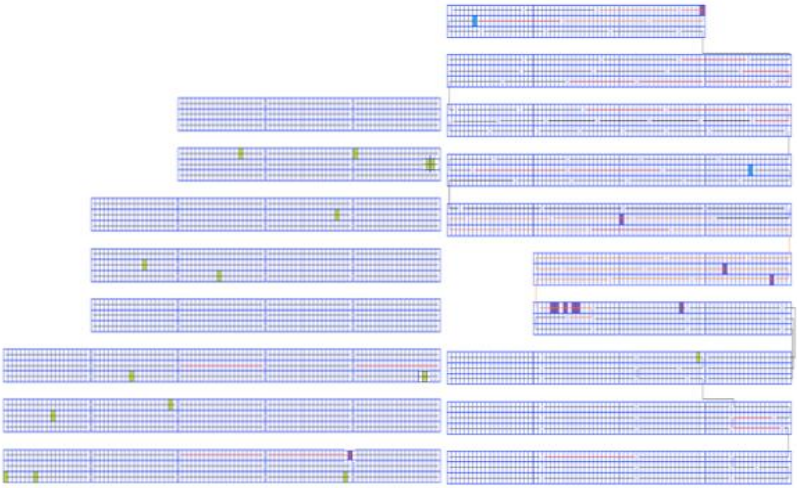


Figure 11 - Infrared image taken with the Aerial IRT-measurement System showing a disconnected PV module string (intermediate, lighter gray-colored row)

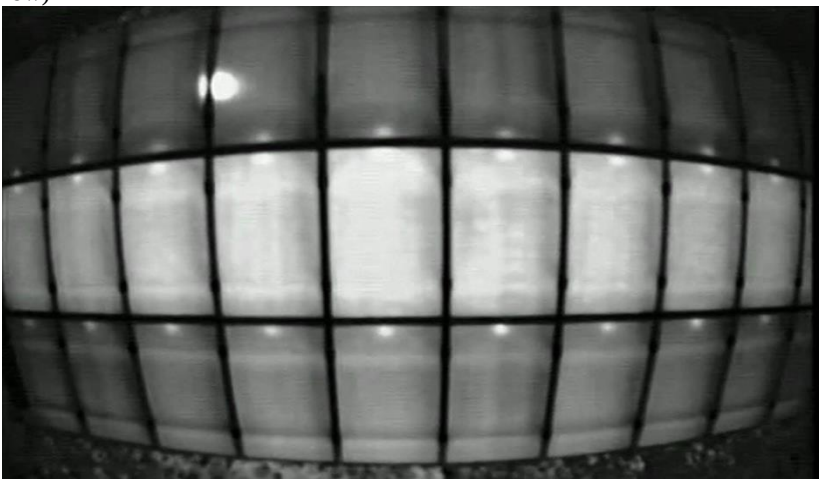


Figure 12 - Infrared image taken with the Aerial IRT-measurement System showing a PV module with hot spots in the lower-right edge of the image.

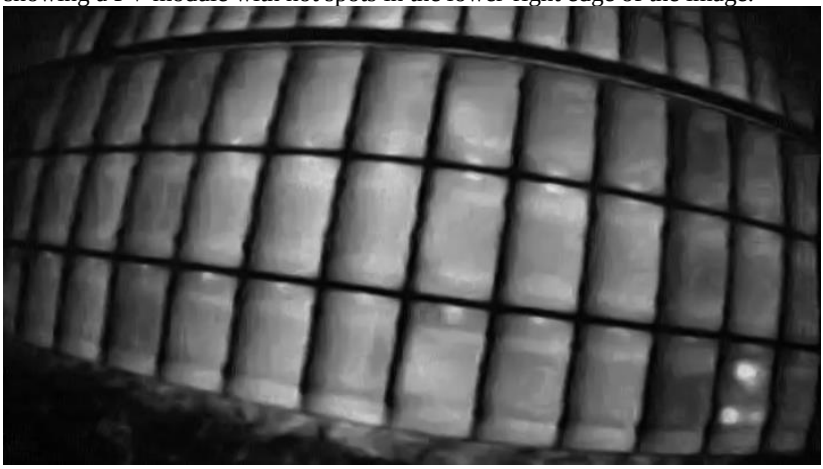


Figure 13 - PV module with two visible cracks, caused by the thermal expansion of the corresponding hot spots.

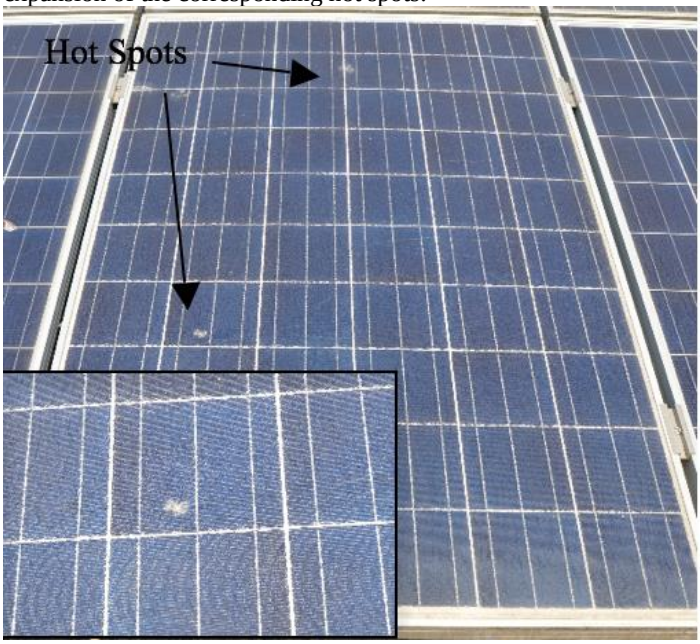
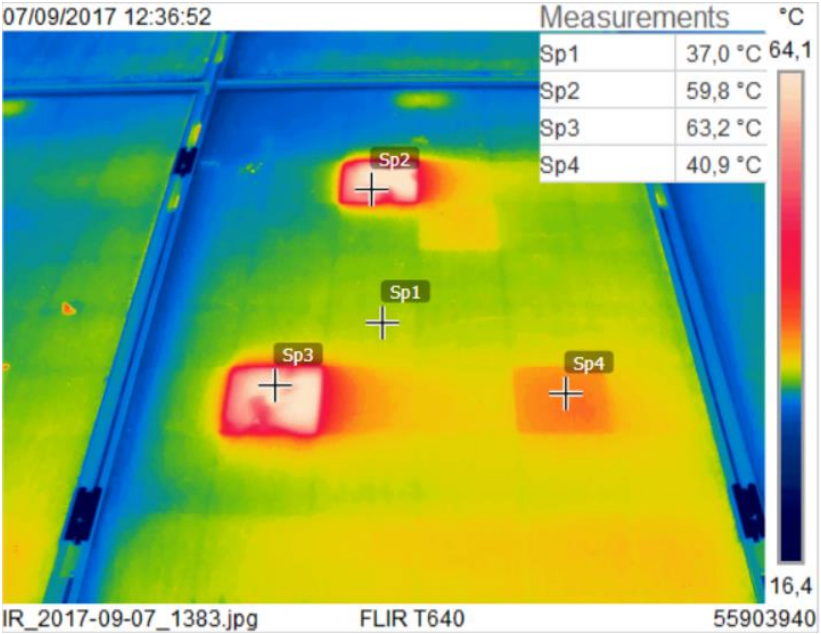


Figure 14 - PV module with a number of hot spot cells: image taken with a hand-held infrared camera (FLIR T640), revealing temperature differences in excess of 26 K.

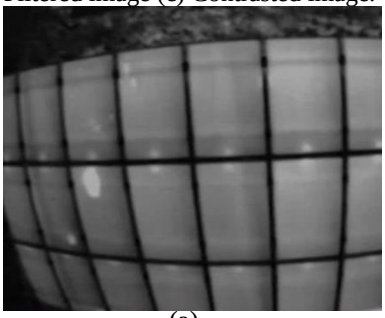


4.2 DIGITAL IMAGE PROCESSING (DIP)

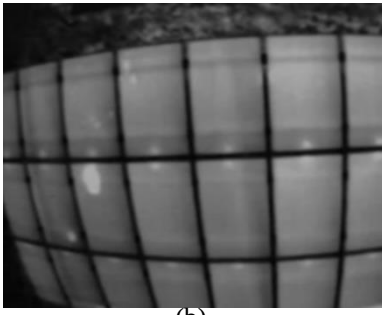
4.2.1 Preprocessing

Using the MATLAB® environment, it was possible to test different parameterizations of the Gaussian filter and the contrast adjustment, to find the best solution to facilitate the segmentation phase. Figure 15 presents an example of an image before and after the preprocessing steps.

Figure 15 - Steps of the preprocessing phase of DIP. (a) Original image (b) Filtered image (c) Contrasted image.



(a)



(b)

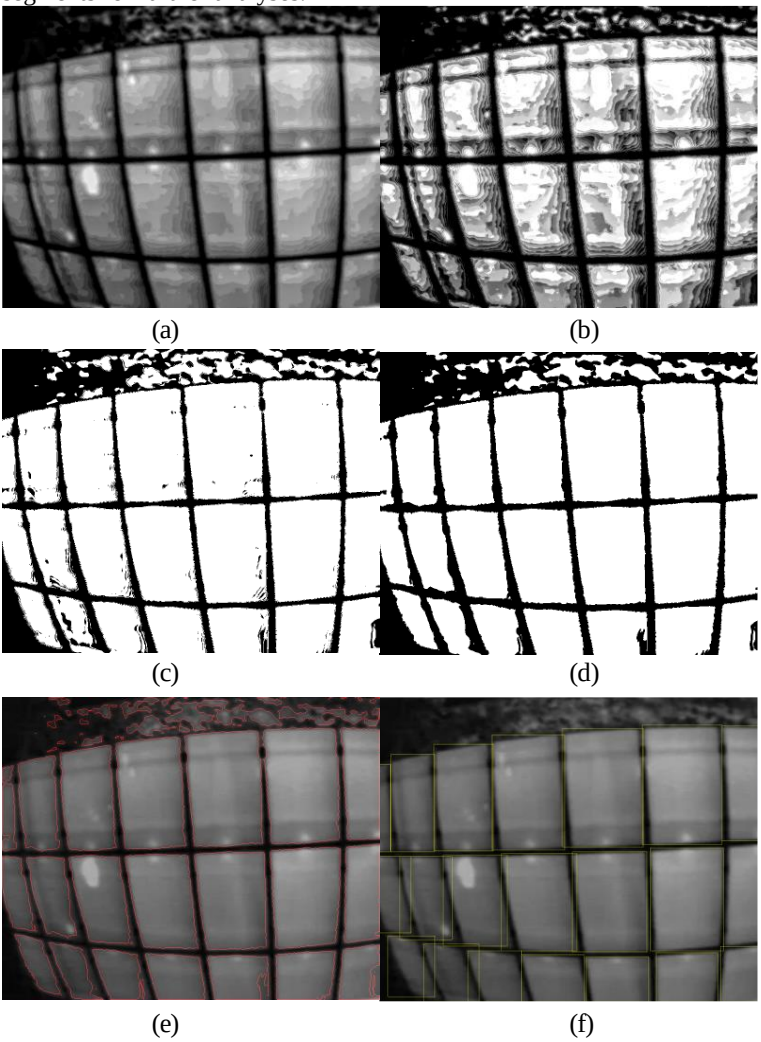


(c)

4.2.2 Segmentation

Figure 16 presents an example of an image showing all the steps of the segmentation process. The Laplacian operator treatment highlights the border of the modules, facilitating the segments detection, which is performed by the binary transformation. Then the segments pass through the hole filling step, which clears the segments, eliminating residual noise. The image is afterwards ready to be separated in segments, which are filtered so that only good quality segments are further analyzed.

Figure 16 - Steps of the segmentation of the images. (a) Preprocessed image (b) Image after Laplacian operator treatment (c) Binary image (d) Binary image with holes filing (e) Border detection (f) Final identification of good quality segments for further analyses.



(a) (b)

(c) (d)

(e) (f)

4.2.3 Classification

After the segmentation, the segments are classified according to Table 6. Figure 17, Figure 18, Figure 19 and Figure 20 show examples of classification of segments of the images analyzed. In Figure 18, the segment in the upper-left corner is not classified, because it is affected by the reflection of the sun on the PV module. All the segments with the same aspect are eliminated from the dataset, in order to avoid confusions with hot spots.

Figure 20 presents some segments with little white spots, which could be erroneously classified as hot spots, but which are actually due to soiling. These PV modules are classified as healthy modules, since soiling is a temporary problem, that is not directly linked to the PV system structure, and are not classified as defects or faults.

Figure 17 - Example of classification of segments of an image with healthy PV modules (marked with number 4), disconnected PV modules (marked with number 1) and a PV module with a bypassed substring (marked with number 3).

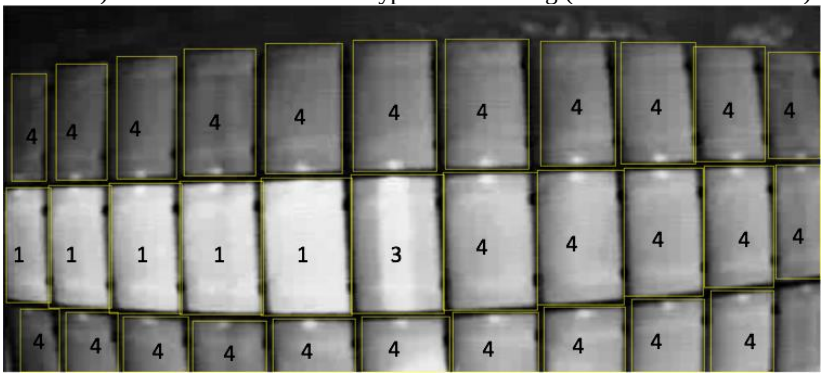


Figure 18 - Example of classification of segments of an image with healthy (marked with number 4) and disconnected (marked with number 1) PV modules.

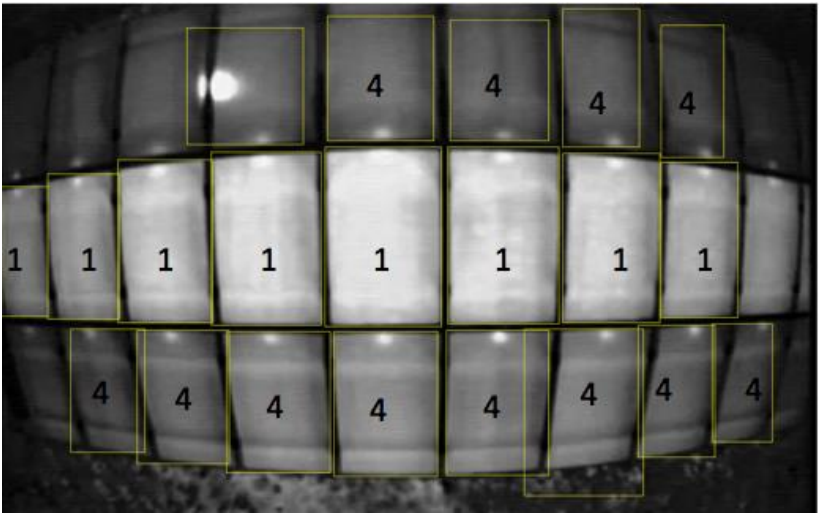


Figure 19 - Example of classification of segments of an image with healthy PV modules (marked with number 4) and PV modules with hot spots (marked with number 2).

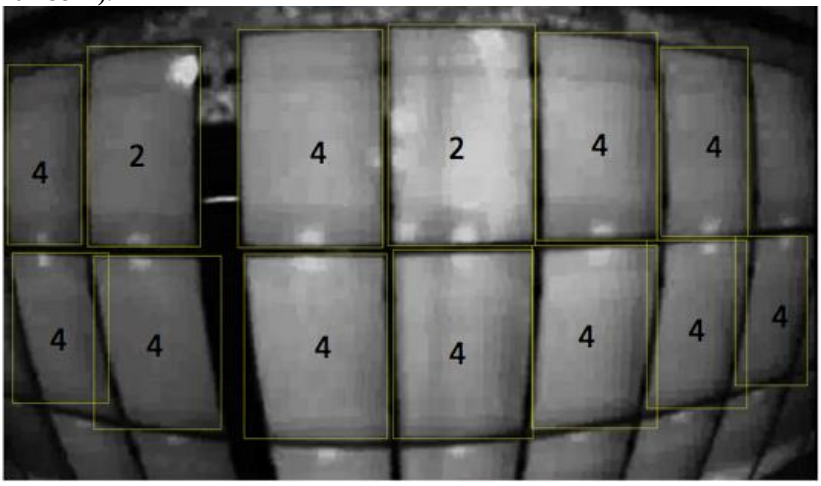
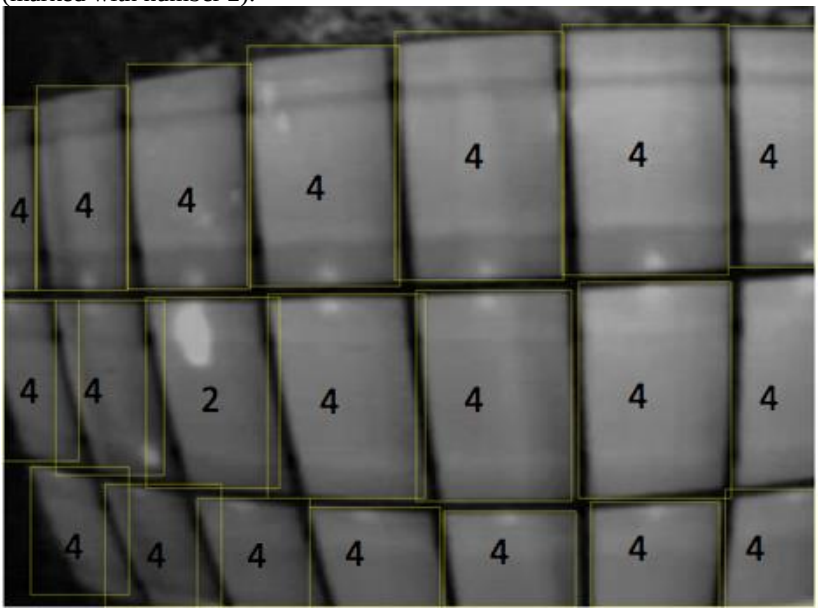


Figure 20 - Example of classification of segments of an image with healthy PV modules (marked with number 4), PV modules with hot spots and soiling (marked with number 2).



To minimize fault diagnosis errors, it is essential to consider the overall pixel luminance characteristics of each segment. The luminance of each pixel of the grayscale image is described by one single Byte which corresponds to 256 levels, 0 for black and 255 for white areas. As presented in (Aghaei et al., 2015; Kim et al., 2017), the infrared images of PV modules with faults have a different pattern of luminance distribution. To compare the differences of luminance characteristics of normal and defective modules, the intensity histograms of the pixels of different segments are compared, as showed in Figure 21, Figure 22, Figure 23 and Figure 24.

Analyzing the images, it is visible that healthy modules (Figure 24) pixels are distributed at an intensity range of 200 or lower and the segments present a histogram pattern similar to a normal distribution. By the other hand, disconnected modules (Figure 21) have a higher concentration of pixels with higher luminance than connected and healthy modules (Figure 24). It is also visible that modules with hot spots (Figure 22) have a small peak of pixel count at higher luminance. Modules with bypassed substrings (Figure 23) present two peaks of pixels at higher

luminance. These peaks cause the deviation of the histograms of defective modules from a normal distribution shape. These differences of intensity distribution range and histogram shape allows a more precise and impartial labeling of the segments.

Figure 21 - Example of luminance distribution for a disconnected PV module

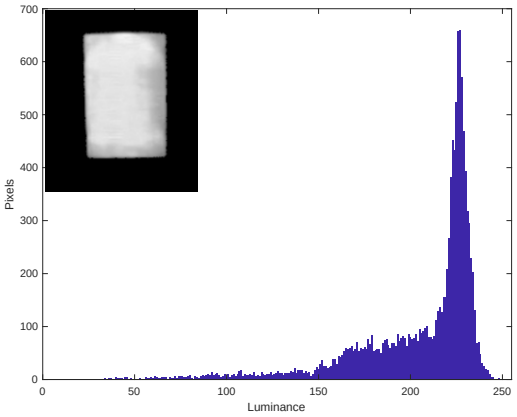


Figure 22 - Example of luminance distribution for a PV module with a hot spot

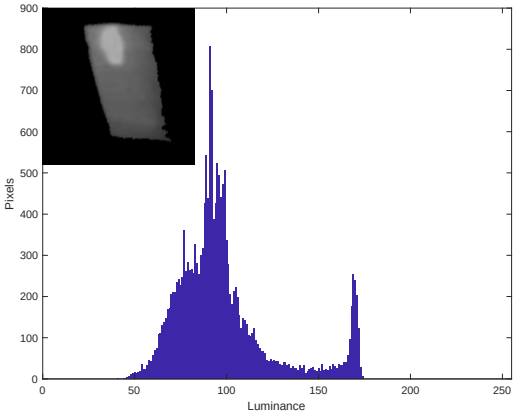


Figure 23 - Example of luminance distribution for a PV module with a bypassed substring

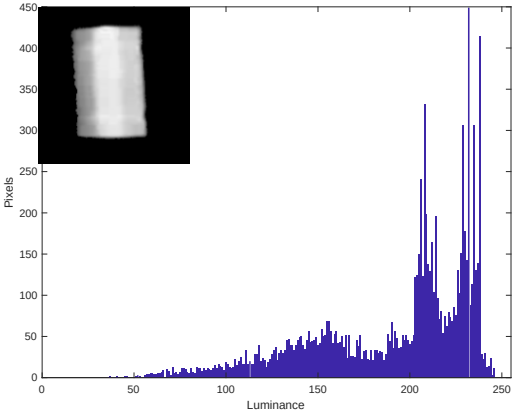
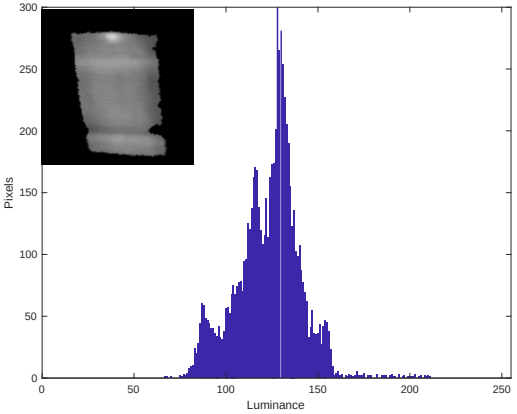
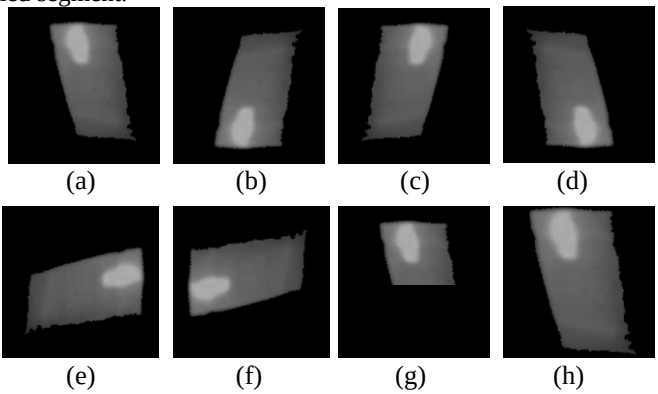


Figure 24 - Example of luminance distribution for a healthy module



As the number of healthy modules segments is much larger than the segments of modules with faults, after labeling the segments, they are augmented. The augmentation artificially enlarges the dataset, as the example of Figure 25, which generated seven new segments by augmenting the original. A larger dataset will improve the overall learning procedure and performance, by feeding the model with varied data.

Figure 25 - Example of segments after augmentation (a) Original segment (b) Horizontal mirrored segment (c) Vertical mirrored segment (d) 180° rotated segment (e) 90° rotated segment (f) 270° rotated segment (g) Croped segment (h) Scaled segment.



(a) (b) (c) (d)

(e) (f) (g) (h)

5 EXPECTED RESULTS AND PRELIMINARY CONCLUSIONS

With the preliminary results, Aerial IRT has proven to be a practical and reliable method to detect faults in large PV plants. Aerial IRT could detect hot spots, bypassed substrings, short-circuited and open-circuited strings in a 3 MWp R&D PV power plant in Brazil. The acquired images were processed with DIP techniques to detect segments of modules that will be used as samples for training the CNN. The final algorithm is expected to successfully identify faulty PV modules and to classify them by their category of faults.

After an extensive and continuing literature review, and to the best of our knowledge, this is the first attempt in the literature to investigate the issue of categorizing of faults in PV power plants using aerial IRT images and CNNs. It is expected that a successful algorithm will represent an important contribution to both the science and technology of solar electricity generation.

6 WORK PLAN AND TIMELINE

Ano	**2018**				**2019**						**2020**						**2021**					
Mês	**5**	**7**	**9**	**11**	**1**	**3**	**5**	**7**	**9**	**11**	**1**	**3**	**5**	**7**	**9**	**11**	**1**	**3**	**5**	**7**	**9**	**11**
Doctoral classes	x	x	x	x	x	x	x															
Finishing of literature review							x	x														
Enlargement of the database of segments of modules with faults	x	x	x	x	x	x	x	x	x	x												
Digital Image Processing of database									x	x	x	x										
Neural Network development													x	x	x							
Training and validation of Neural Network																x	x					
Elaboration of results of the artificial neural network training and validation																		x	x			
Conclusion																				x		
Review and finalization of the thesis																					x	
Thesis presentation																						x

REFERENCES

ABSOLAR. (n.d.). Brasil ultrapassa 1 GW em usinas solares em operação, diz associação do setor. Retrieved January 20, 2018, from http://absolar.com.br/noticia/noticias-externas/brasil- ultrapassa-1-gw-em-usinas-solares-em-operacao-diz- associacao-do-setor.html

Aghaei, M. (2016). *Novel methods in control and monitoring of photovoltaic systems*. POLITECNICO DI MILANO.

Aghaei, M., Leva, S., Grimaccia, F., & Milano, P. (2016). PV Power Plant Inspection by Image Mosaicing Techniques For IR Real-Time Images, 3100–3105.

Aghaei, M., Member, S., Grimaccia, F., Gonano, C. A., Leva, S., & Member, S. (2015). Innovative Automated Control System for PV Fields Inspection and Remote Control. *IEEE TRANSACTIONS ON INDUSTRIAL ELECTRONICS*, *62*(11), 7287–7296.

Andrews, R. (2018). Aerial inspections for solar asset optimization. *Solar Asset Management*.

Bagnall, D. M., & Boreland, M. (2008). Photovoltaic technologies. *Energy Policy*, *36*(12), 4390–4396. https://doi.org/10.1016/j.enpol.2008.09.070

Buerhop, C., Schlegel, D., Niess, M., Vodermayer, C., Weißmann, R., & Brabec, C. J. (2012). Reliability of IR-imaging of PV-plants under operating conditions. *Solar Energy Materials and Solar Cells*, *107*, 154–164. https://doi.org/10.1016/j.solmat.2012.07.011

Canena, & Ângeluz da Costa. (2012). *Redes Neurais Artificiais Dinâmicas Aplicadas a Detecção Automática de Eventos Comportamentais*. Universidade Federal de Santa Catarina.

Carneiro, A. C., & Silva, R. R. V. (2017). Redes Neurais Convolucionais com Tensorflow: Teoria e Prática. In *III Escola Regional de Informática do Piauí* (pp. 382–406).

Djordjevic, S., Parlevliet, D., & Jennings, P. (2014). Detectable faults on recently installed solar modules in Western Australia. *Renewable Energy*, *67*, 215–221. https://doi.org/10.1016/j.renene.2013.11.036

Filho, O. M., & Neto, H. V. (1999). *Processamento Digital de Imagens*. *Revista Brasileira de Geofísica* (Vol. 21/03). https://doi.org/10.1590/S0102-261X1998000100035

Frazão, M., Silva, J. A., Lobato, K., & Serra, J. M. (2017). Electroluminescence of silicon solar cells using a consumer grade digital camera, *99*, 7–12. https://doi.org/10.1016/j.measurement.2016.12.017

Geng, Q., Zhou, Z., & Cao, X. (2018). Survey of recent progress in semantic image segmentation with CNNs. *Science China Information Sciences*, *61*(5), 1–18. https://doi.org/10.1007/s11432-017-9189-6

Gonzalez, R., & Woods, R. (2002). *Digital image processing*. *Prentice Hall*. https://doi.org/10.1016/0734-189X(90)90171-Q

Grimaccia, F., Aghaei, M., Mussetta, M., Leva, S., & Quater, P. B. (2015). Planning for PV plant performance monitoring by means of unmanned aerial systems (UAS), 47–54. https://doi.org/10.1007/s40095-014-0149-6

International Electrotchnical Commission (IEC). (2017). IEC TS 62446-3 - Photovoltaic (PV) systems - Requirements for testing, documentation and maintenance - Part 3: Photovoltaic modules and plants - Outdoor infrared thermography. Geneva.

IRENA. (2017). *Boosting Solar PV Markets : The Role of Quality Infrastructure*. Abu Dhabi.

John A. Tsanakas, Godefroy Vannier, Alexandre Plissonnier, Duy Long Ha, F. B. (2016). Fault Diagnosis and Classification of Large-Scale Photovoltaic Plants through Aerial Orthophoto Thermal Mapping. In *31st European Photovoltaic Solar Energy Conference and Exhibition attached* (pp. 1783–1788).

Junior, C. F. C. (2011). *Uso de descritores morfológicos e cinemáticos na identificação automática de comportamentos de animais de laboratório*. Universidade Federal de Santa Catarina.

Kamilaris, A., & Prenafeta-Boldú, F. X. (2018). Deep Learning in Agriculture: A Survey. *Computers and Electronics in Agriculture*, *147*(1), 70–90. https://doi.org/10.1016/j.compag.2018.02.016

Kim, D., Youn, J., & Kim, C. (2016). Automatic Detection of Malfunctioning Photovoltaic Modules Using Unmanned Aerial Vehicle Thermal Infrared Images. *Journal of the Korean Society of Surveying, Geodesy, Photogrammetry and Cartography*, *34*(6), 619–627. https://doi.org/10.7848/ksgpc.2016.34.6.619

Kim, D., Youn, J., & Kim, C. (2017). Automatic fault recognition of photovoltaic modules based on statistical analysis of UAV thermography. *International Archives of the Photogrammetry, Remote Sensing and Spatial Information Sciences - ISPRS Archives*, *42*(2W6), 179–182. https://doi.org/10.5194/isprs-archives-XLII-2-W6-179-2017

Köntges, M., Kurtz, S., Packard, C. E., Jahn, U., Berger, K., Kato, K., … Van Iseghem, M. (2014). *Review of Failures of Photovoltaic Modules*. *IEA-Photovoltaic Power Systems Programme*. https://doi.org/978-3-906042-16-9

Krizhevsky, A., Sutskever, I., & Hinton, G. E. (2012). ImageNet Classification with Deep Convolutional Neural Networks. *Advances In Neural Information Processing Systems*, 1–9. https://doi.org/http://dx.doi.org/10.1016/j.protcy.2014.09.007

Kropp, T., Berner, M., Stoicescu, L., & Werner, H. (2017). Self-Sourced Daylight Electroluminescence From Photovoltaic Modules, *7*(5),

1184–1189.

Lecun, Y., Bengio, Y., & Hinton, G. (2015). Deep learning. *Nature*, *521*(7553), 436–444. https://doi.org/10.1038/nature14539

Leva, S., Aghaei, M., & Grimaccia, F. (2015). PV Power Plant Inspection by UAS : Correlation between Altitude and Detection of Defects on PV Modules.

Malof, J. M., Bradbury, K., Collins, L. M., & Newell, R. G. (2016). A Deep Convolutional Neural Network and a Random Forest Classifier for Solar Photovoltaic Array Detection in Aerial Imagery. *International Conference on Renewable Energy Research and Applications (ICRERA)*, *5*, 650–654. https://doi.org/10.1109/ICRERA.2016.7884415

Mayo, R. C., & Leung, J. (2018). Artificial intelligence and deep learning – Radiology's next frontier? *Clinical Imaging*, *49*(July 2017), 87–88. https://doi.org/10.1016/j.clinimag.2017.11.007

Mehta, S., Azad, A. P., Chemmengath, S. A., Raykar, V., & Kalyanraman, S. (2017). DeepSolarEye: Power Loss Prediction and Weakly Supervised Soiling Localization via Fully Convolutional Networks for Solar Panels, *1*(d). Retrieved from http://arxiv.org/abs/1710.03811

Munoz, M. A., Alonso-García, M. C., Vela, N., & Chenlo, F. (2011). Early degradation of silicon PV modules and guaranty conditions. *Solar Energy*, *85*(9), 2264–2274. https://doi.org/10.1016/j.solener.2011.06.011

Parida, B., Iniyan, S., & Goic, R. (2011). A review of solar photovoltaic technologies. *Renewable and Sustainable Energy Reviews*, *15*(3), 1625–1636. https://doi.org/10.1016/j.rser.2010.11.032

Quater, P. B., Grimaccia, F., Leva, S., Mussetta, M., & Aghaei, M. (2014). Light Unmanned Aerial Vehicles (UAVs) for cooperative inspection of PV plants. *IEEE Journal of Photovoltaics*, *4*(4), 1107–1113. https://doi.org/10.1109/JPHOTOV.2014.2323714

Renganathan, R. M. V., Natarajan, V., & Jahaagirdar, T. (2016). Failure mechanism in PV systems. *Graduate Course MAE 598: Solar Commercialization*, 1–17. Retrieved from http://roedel.faculty.asu.edu/sec598s16/assignments/fp_reports/T12report.pdf

Rogotis, S., Ioannidis, D., Tsolakis, a, Tzovaras, D., & Likothanassis, S. (2014). Early defect diagnosis in installed PV modules exploiting spatio-temporal information from thermal images. *QIRT2014 Conférence*.

Rüther, R. (2004). *Edifícios solares fotovoltaicos: o potencial da geração solar fotovoltaica integrada a edificações urbanas e interligada à rede elétrica pública no Brasil*. *Ufsc-Labsolar*.

The, S., Ai, S., Dalle, I., & Galleria, S. (2014). Deep Learning in Neural

Networks : An Overview, 1–88.

Thermoteknix. (2018). MicroCAM 2 ™ Datasheet. Retrieved March 15, 2018, from http://www.thermoteknix.com/wp-content/uploads/2013/08/MicroCAM-2-Brochure.pdf

Tsanakas, J. A., & Botsaris, P. N. (2012). An infrared thermographic approach as a hot-spot detection tool for photovoltaic modules using image histogram and line profile analysis. *International Journal of Condition Monitoring*, *2*(1), 22–30. https://doi.org/10.1784/204764212800028842

VATh. (2016). Electrical Infrared Inspections ▪ Low Voltage, (February), 17.

Voulodimos, A., Doulamis, N., Doulamis, A., & Protopapadakis, E. (2018). Deep Learning for Computer Vision: A Brief Review. *Computational Intelligence and Neuroscience*, *2018*, 1–13. https://doi.org/10.1155/2018/7068349

Weinreich, B., Haas, R., Zehner, M., & Becker, G. (2011). Optimierung thermografischer Fehleranalyseverfahren auf Multi-MW-PV-Kraftwerke. *26th PV-Symposium Bad Staffelstein*, (1), 10.

Zhang, S., Wu, G., Yang, X., Jiang, W., & Zhou, J. (2017). Digital image-based identification method for the determination of the particle size distribution of dam granular material. *KSCE Journal of Civil Engineering*, *0*(0), 1–14. https://doi.org/10.1007/s12205-017-0304-8

Zilles, R. (2012). *Sistemas fotovoltaicos conectados à rede elétrica* (Vol. 16). São Paulo: Oficina dos Textos.

APPENDIX A – SPREADSHEET FOR THE RECORD OF THE UAV FLIGHT



fotovoltaicaufsc

Date:	
Client data:	**PV Plant**
Operator:	Localization:
Equipment	Nominal rated power (kW):
Model UAV:	Workload (%):
Weight:	PV Modules (#, model
Camera (sensibility, resolution):	
Flight Log Number _____	
Route	**Time:**
	Height:
	Angle of the camera:
	Weather conditions (irradiance, wind speed, cloud coverage):
	String/Table:
Found faults:	**Experimental Artifacts:**